

Article

An Optimized Vector Tracking Architecture for Pseudo-Random Pulsing CDMA Signals

Lin Tao, Guangchen Li , Junren Sun and Bocheng Zhu *

School of Electronics Engineering and Computer Science, Peking University, Beijing 100871, China; taolin_yiran@pku.edu.cn (L.T.); liguangchen@pku.edu.cn (G.L.); sunjunren@pku.edu.cn (J.S.)

* Correspondence: zhucb@pku.edu.cn; Tel.: +86-139-1188-7720

Abstract: The vector tracking loop (VTL) has high tracking accuracy and a superior ability to track weak signals in GNSS. However, traditional VTL architecture is established on continuous Code Division Multiple Access (CDMA) signal and is incompatible with pseudolite positioning systems (PLPS) because PLPS generally adopts a pseudo-random pulsing CDMA signal structure to mitigate the near-far effect. Therefore, this paper proposes an optimized VTL architecture for pseudo-random pulsing CDMA signals. To avoid estimation biases in PLPS, the proposed VTL adopts irregular update periods (IUP) pre-filters which adjust the update cycles according to the active timeslot intervals. Meanwhile, as the active timeslots of different pseudolites do not overlap, the sampling time of the navigation filter inputs is inconsistent and time-varying, causing jitter degradation. Thus, the proposed VTL predicts the measurements so that they can be sampled at the same time, which improves tracking accuracy. Simulation is carried out to evaluate the performance of the proposed VTL. The results suggest that the proposed VTL outperforms the traditional pre-filter-based VTL and IUP pre-filter-based VTL.



Citation: Tao, L.; Li, G.; Sun, J.; Zhu, B. An Optimized Vector Tracking Architecture for Pseudo-Random Pulsing CDMA Signals. *Sensors* **2021**, *21*, 4087. <https://doi.org/10.3390/s21124087>

Academic Editors: Kamil Krasuski and Damian Wierzbicki

Received: 12 May 2021
Accepted: 7 June 2021
Published: 14 June 2021

Publisher's Note: MDPI stays neutral with regard to jurisdictional claims in published maps and institutional affiliations.



Copyright: © 2021 by the authors. Licensee MDPI, Basel, Switzerland. This article is an open access article distributed under the terms and conditions of the Creative Commons Attribution (CC BY) license (<https://creativecommons.org/licenses/by/4.0/>).

Keywords: pseudo-random pulsing signal; irregular update periods; predicted measurement; vector tracking loop

1. Introduction

The Global Navigation Satellite System (GNSS) has been considered the first alternative to provide real-time positioning, navigation, and timing (PNT) services worldwide. Despite the benefit of broad coverage, high accuracy, and low cost, the GNSS-based PNT systems are fragile in challenging scenarios, such as deep valleys, heavily forested areas, open-cut mines, urban canyons, and even indoors [1,2]. Therefore, much research has been carried out to improve GNSS availability and robustness in these challenging environments [3,4]. The studies can be separated into two directions. One is to improve the performance of GNSS systems [3], such as adopting more advanced signal structures [5,6], applying anti-jamming receiving technologies [7], and enhancing signal power. The other is to design new positioning systems suitable for the ground [4,8], such as ultra-wideband [9], Wi-Fi [10], 4G or 5G [11], and pseudolite-based positioning technologies [12–14]. Due to the benefits of the great flexibility, easy servicing, broad signals coverage, compatibility with GNSS, and high positioning precision, the pseudolite positioning system has attracted increasing attention in recent years.

Pseudolites are ground-based satellites transmitting GNSS-like signals. The positioning precision and continuity of the GNSS can effectively be improved by installing pseudolites in urban areas, indoors, and in scenarios where the GNSS is problematic. Simultaneously, pseudolites can also be used to offer continuous and reliable positioning services to users as an independent positioning system. However, the Pseudolites Positioning Systems (PLPS) suffers severely from the near-far effect [15,16]. The near-field pseudolites may interfere with far-field signals when the receiver moves close to a pseudolite, causing

failure to track and synchronize the distant pseudolite signal, referred to as the near-far effect [16]. Various techniques have been proposed for alleviating the near-far effect, including frequency hopping [17], new spreading codes [15] pulse modulation [18], and optimizing pseudolite antenna [19]. However, the preferred one is to pulse the pseudolite signals in pseudo-random because of the low resource cost and good resistance to the near-far effect.

As the name indicates, the pulse signals could be regarded as gated direct sequence spread spectrum (DSSS) signals. Each pseudolite transmits signals at different timeslots, preventing mutual interference. Although the pulse signal with equal intervals is easier to realize, it may result in sub-peaks in the frequency domain, causing false frequency-lock in the receiver [20,21]. Thus, the pseudo-random pulse scheme should be adopted in PLPS. Some literature [18,22,23] offer different designs of the pulse scheme. The cornerstone of these schemes is to use a pseudo-random pulse sequence to control pseudolite pulse signal transmission.

The pseudo-random pulse signal (PRPS) brings some challenges in tracking compared to GNSS signals. It would increase the measurement noise and decrease the tracking convergence speed if the receiver tracks the PRPS according to the traditional tracking architecture. A tracking loop architecture of conventional PLL and delay lock loop (DLL) pre-cascaded with a Noise Silencer Module (NSM) is proposed in Reference [24]. This tracking loop is turned on only when the valid timeslot of the signal arrives. It mitigates the interference of other pseudolite signals and reduces noise accumulation when the signal is silent. Because the intervals between two adjacent valid timeslots are pseudo-random, the discriminator of the NSM-PLL/DLL tracking loop has a bias in estimating the carrier phase and code phase, reducing the tracking accuracy of the loop. Therefore, Yun et al. propose a variable update rate carrier tracking loop based on the Kalman filter (KF-VURL) [25], which effectively solves the estimation bias problem of the discriminator. In estimating the carrier phase and doppler, the KF-VURL shows higher tracking accuracy and faster convergence.

Though much research on pseudolite tracking focuses on improving and optimizing the scalar tracking loop (STL) [24–27], they ignore the abundant information of other channels. In contrast, the VTL uses a big loop to filter the observations of all channels, which makes full use of the information of each channel and improves the tracking performance of the signals. Initially, the VTL was introduced by Spilker [28] and popularly developed in recent years, mainly applied in GNSS. The VTL algorithm can track weak signals, which increases the number of visible satellites and, thus, has better performance in harsh environments [29]. Furthermore, the VTL algorithm utilizes other normal operation tracking channels to predict and compensate for the observations of momentary outage signals to maintain continuous tracking [30].

The typical types of VTL include vector delay lock loop (VDLL) [30–32], vector frequency lock loop (VFLL) [31,32], vector delay frequency lock loop (VDFLL) [32–34], and vector phase lock loop (VPLL) [35]. Hyounghmin So et al. propose a VTL algorithm applicable to asynchronous PLPS, significantly mitigating the near-far problem [36]. However, its VTL is still based on the continuous GNSS signal model, ignoring the pseudo-random pulsing characteristic of pseudolite signals. The measurement inputs of the navigation filter in traditional VTL are discriminator outputs in each channel, and the navigation filter obtains the errors at similar sampling time. Nevertheless, this structure is not appropriate for the vector tracking of pseudolite signals. The reasons are as follows. Firstly, the output of the discriminator can only reflect the errors before the valid timeslot due to the pulse feature of PRPS. Secondly, as the active timeslots of different pseudolites do not overlap, the output time of each channel discriminator is different.

The structure based on the pre-filters and navigation filter provides a possible solution to these problems in tracking pseudolite signals because, by improving the architecture of pre-filters, the robustness of VTL would be enhanced, and its application scope could be expanded. Unfortunately, the application of pre-filter-based VTL mainly focuses on GNSS

signals. Jin et al. present a federal tracking loop consist of subfilters in every channel and a master filter [37]. By adding subfilters, the computational complexity of VTL is effectively reduced, and the robustness is also enhanced, while the tracking performance is almost unchanged. The pre-filters in the VTL proposed by Xie et al. are based on the unscented Kalman filter (UKF) and directly operate on the in-phase and quadra-phase correlator outputs to obtain the phase and frequency biases [38]. However, these pre-filters are based on the continuous GNSS model, causing jitter degradation when tracking PRPS.

To solve the problems in tracking PRPS, an optimized VTL architecture that includes irregular update periods (IUP) pre-filters and a navigation filter based on predicted measurements (PM) is proposed. The proposed VTL is abbreviated as IUPPM-VTL. According to the timeslot intervals, the IUP pre-filter based on the Kalman filter (KF) adjusts the update cycles, avoiding the impact of the pseudo-random pulsing signal. So, it can estimate the measurement accurately. However, since the pre-filters are updated at varying timeslots and not consistent with each other, using them directly as the inputs of the navigation filter would increase the vector tracking estimation noise. As a consequence, the IUPPM-VTL predicts the measurements so that they can be to sampled at the same time. Meanwhile, this paper compares the proposed IUPPM-VTL with traditional VTL based on pre-filter and IUP-VTL based on IUP-prefilter.

The rest of this paper is organized as follows. Section 2 introduces the PRPS structure. Section 3 describes the problems in tracking PRPS. Section 4 proposes the optimized VTL architecture. The simulation and comparison testing are carried out in Section 5. Conclusions and future work are summarized in Section 6.

2. Pseudo-Random Pulsing Signal Structure

The signal structure of PRPS is first introduced. The pseudolite positioning system is a ground-based satellite navigation system that uses a low-cost launcher to transmit GNSS-like signals. Therefore, the pseudolite system relies on the spreading code to achieve terminal equipment positioning functions. The difference is that the pseudolite signal adopts the pulsing signal structure to overcome the near-far effect. Figure 1 shows the modulation process of PRPS, which is equivalent to the pulse modulation of a continuous CDMA signal.

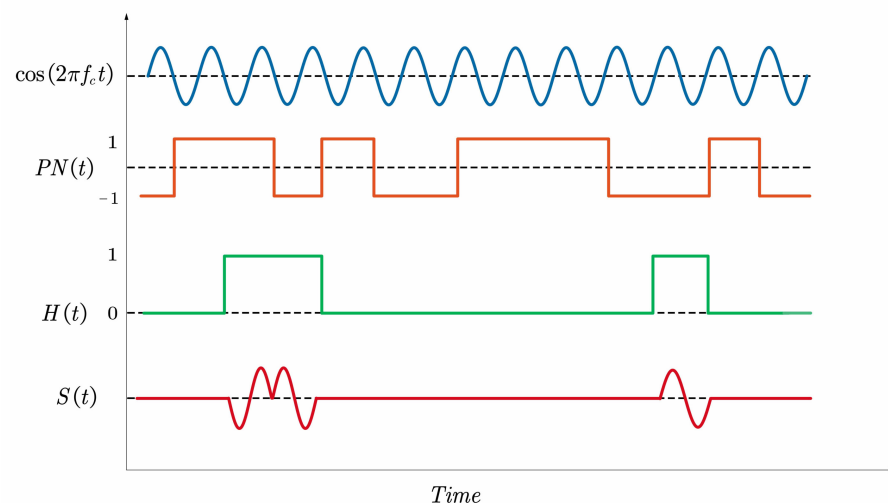


Figure 1. Schematic diagram of PRPS modulation.

The mathematical model of the received pseudo-random pulsing signal is expressed by the following formula.

$$S^i(t) = \left[A^i D^i(t) P N^i(t - \tau^i) \cos\left(2\pi(f_{IF} + f_d^i)t + \varphi_0^i\right) \right] \cdot H^i(t - \tau^i), \quad (1)$$

where $H^i(t)$ is the pulse modulation sequences. The pseudo-random code for the i -th pseudolite A^i represents amplitude of the received signal, $D^i(t)$ denotes the modulated data bits, τ^i is the i -th transmitter-receiver time delay, f_d^i is the doppler shift, and f_{IF} and ϕ_0^i are the intermediate frequency (IF) and initial carrier phase, respectively.

The pulse signal $H^i(t)$ at the i -th transmitter is repeated by the basic pulse scheme $h_0^i(t)$, which can be modeled as follows:

$$H^i(t) = \sum_{m=0}^{+\infty} h_0^i(t - mT_p), \quad (2)$$

where T_p represents the repetition period of $h_0^i(t)$, which can be expressed as:

$$h_0^i(t) = \sum_{k=0}^{N_f-1} \Omega(t - kT_f - c_k^i T_s). \quad (3)$$

$\Omega(t)$ is the single square wave function, which is

$$\Omega(t) = \begin{cases} 1, & t \in [0, T_s) \\ 0, & \text{otherwise} \end{cases}. \quad (4)$$

In Equation (3), T_s denotes the duration of timeslot, T_f is one frame time which is equal to $N_s T_s$, and N_s is the number of timeslots in one frame. The pulse duty cycle d is $1/N_s$, and N_f indicates the frame number of the basic pulse pattern, so $T_p = N_f T_f$. c_k^i represents the pulse position index in k -th frame. Meanwhile, c_k^i satisfies the following two requirements:

1. The value of c_k^i ranges from 0 to $N_s - 1$.
2. The active timeslots of different pseudolites do not overlap.

Generally, c_k^i is a pseudo-random permutation. It ensures the pulse pseudolite signal has better spectral properties, described in detail in Reference [18]. The pseudolite transmits signals in active timeslots where $H^i(t)$ is 1 and keeps silent in silent timeslots where $H^i(t)$ is 0. Thus, the pseudolite signals would not interfere with each other. The transmitting time of the pulse signal is time-varying and predetermined by a pseudo-random permutation.

An illustration of the pulse pattern is shown in Figure 2. The horizontal axis represents timeslot index c_k^i ranging from 0 to $N_s - 1$ in one frame, and the vertical axis represents the frame index k ranging from 0 to $N_f - 1$. The green squares represent the active timeslots indexes.

i -th Pseudolite		Timeslot Index c_k^i							
		0	1	2	...	N_s-3	N_s-2	N_s-1	
Frame Index k	0				...				
	1								
	2								
							
	N_f-3								
	N_f-2								
	N_f-1								

Figure 2. Illustration of the pulse pattern.

3. Problem Description

Based on the PRPS structure, this section analyzes the problems existing in the vector tracking process of pseudolite signals. The local replica $S_r^i(t)$ of i -th pseudolite is defined as:

$$S_r^i(t) = PN_r^i(t) \cos(2\pi f_r t) \cdot H_r^i(t), \quad (5)$$

where PN_r^i represents the spreading code replica, H_r^i denotes the pseudo-random pulsing signal replica, and f_r is the frequency of local replica.

The in-phase (I) integration of prompt correlator can be described in the following formula when the receiver tracks the signal of i -th pseudolite.

$$\begin{aligned} I_p(k) &= \frac{1}{T_s} \int_{t_k}^{t_k+T_s} S^i(t) \cdot S_r^i(t) dt \\ &= AD(k)R(\Delta\tau_k) \operatorname{sinc}(\Delta f_k T_s) \cos \left[2\pi\Delta f_k \left(t_k + \frac{1}{2}T_s \right) + \Delta\phi_0 \right] + n_I' \end{aligned} \quad (6)$$

where $\Delta\tau_k$ and Δf_k denote the code phase and the frequency errors between the received signal and the local replica in the current epoch, respectively. $\Delta\phi_0$ is the initial carrier phase error. $R(\cdot)$ is the autocorrelation value of the spreading code, T_s is timeslot period, and n_I indicates the in-phase noise. The starting integration time t_k is

$$t_k = kT_f + c_k^i T_s = (kN_s + c_k^i) \cdot T_s. \quad (7)$$

The prompt quadra-phase (Q) integration of prompt correlator can be expressed as:

$$Q_p(k) = AD(k)R(\Delta\tau_k) \operatorname{sinc}(\pi\Delta f_k T_s) \sin \left[2\pi\Delta f_k \left(t_k + \frac{1}{2}T_s \right) + \Delta\phi_0 \right] + n_Q. \quad (8)$$

The average carrier phase error measured by the discriminator is as follows.

$$\overline{\Delta\phi_k} = \arctan \left(\frac{Q_p}{I_p} \right) \simeq 2\pi\Delta f_k \left(t_k + \frac{1}{2}T_s \right) + \Delta\phi_0. \quad (9)$$

The discriminator output approximates the average phase error between the received signal and the local replica in the active timeslot, as defined in Equation (9). Thus, $\overline{\Delta\phi_k}$ is affected by Δf_k , T_s , $\Delta\phi_0$, and t_k . Since the tracking process replicates the signal parameters by filtering the discriminator outputs, it is vital to establish an appropriate output model. For simple analysis, this paper supposes that the tracking loop does not feedback the estimations to NCO. Thus, Δf_k would be constant in this process. $\Delta\phi_0$ is the initial carrier phase error, and T_s is the timeslot period. Both of them are constant, while t_k is varying. Hence, it is necessary to focus on the analysis of the influence of t_k on $\overline{\Delta\phi_k}$. Within each tracking period, the variation of carrier phase discriminator output can be expressed as:

$$\nabla\overline{\Delta\phi_k} = \overline{\Delta\phi_k} - \overline{\Delta\phi_{k-1}} = 2\pi\Delta f_k T_{k-1}, \quad (10)$$

where

$$T_{k-1} = t_k - t_{k-1} = (N_s + c_k^i - c_{k-1}^i) \cdot T_s. \quad (11)$$

T_{k-1} represents the intervals between the last active timeslot and the currently active timeslot, which is time-varying and predetermined by the pseudo-random permutation. However, for continuous CDMA signal, T_{k-1} is equal to the constant correlation integration time T_f . The difference of $\nabla\overline{\Delta\phi_k}$ in tracking continuous CDMA signal and PRPS is shown in Figure 3.

The horizontal axis in Figure 3 represents the time, and the vertical axis represents the frequency error, so the shaded area represents $\nabla\overline{\Delta\phi_k}$ (ignoring the scaling factor 2π). The $\nabla\overline{\Delta\phi_k}$ is time-invariant in tracking continuous CDMA signal shown in Figure 3a. Thus, with a fixed update period, the traditional tracking loop could accurately estimate

and correct the frequency error, whereas Figure 3b shows that, when tracking PRPS, the $\nabla\Delta\phi_k$ is time-variant because of T_{k-1} . It is supposed that the time-varying property of T_k is ignored in the tracking loop design. In that case, the frequency error cannot be accurately estimated, resulting in jitter degradation of tracking performance, which is also described in Reference [25].

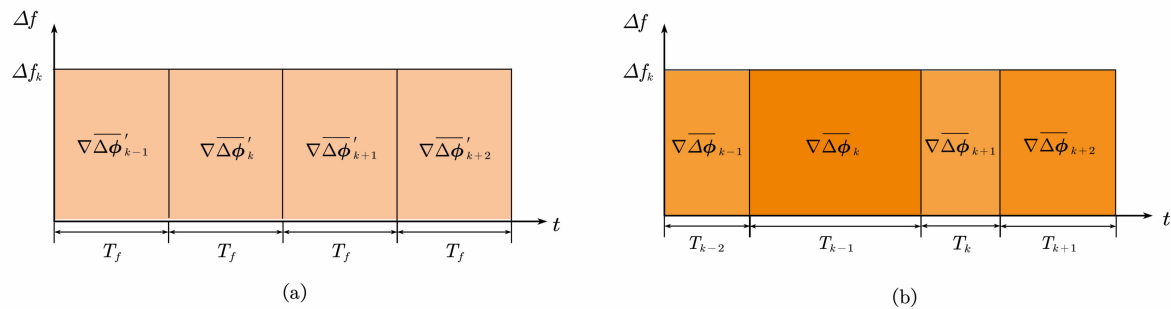


Figure 3. The comparison between $\nabla\Delta\phi_k$ in tracking continuous CDMA signal and PRPS. (a) $\nabla\Delta\phi'_k$ of tracking continuous CDMA signal; (b) $\nabla\Delta\phi_k$ of tracking PRPS.

Similarly, the code phase discriminator output is also time-varying as the code phase error is driven by the same, albeit scaled, dynamics as the carrier phase over short time intervals [39]. The variation of code phase discriminator output is

$$\begin{aligned}\nabla\Delta\tau_k &= \beta\Delta f_k T_{k-1} \\ \beta &= \frac{f_{code}}{f_c},\end{aligned}\quad (12)$$

where f_{code} indicates the frequency of spreading code.

According to Equations (9), (10), and (12), the error parameter is related to the time intervals T_{k-1} of adjacent effective timeslots. These parameters can be accurately estimated by designing a scalar tracking loop of variable update period, as researched in Reference [24,25,27].

In the vector tracking structure, the input observations of the navigation filter need to be sampled simultaneously. However, the estimation time of the errors in each channel is inconsistent and time-varying in PLPS. Figure 4 depicts this problem. The dotted arrows represent the navigation filter sampling time, while the solid arrows indicate the error estimation time in each channel. Unfortunately, there exists a time difference between them. Therefore, the input observations of the navigation filter cannot reflect the errors during this time (gray shaded part). Even worse, this time difference is pseudo-random, causing jitter degradation of the navigation filter when using conventional VTL loops to track PRPS. Hence, it is necessary to design the VTL according to the characteristics of the PRPS.

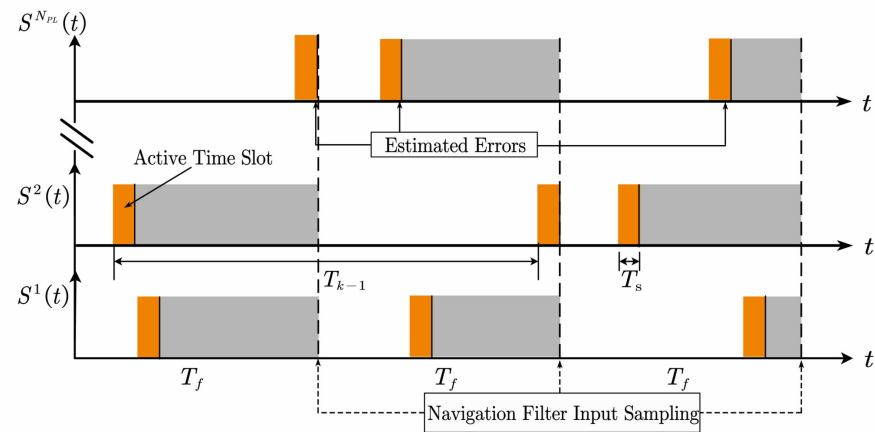


Figure 4. Schematic diagram of input sampling for navigation filter.

4. The Proposed VTL Architecture

Based on the analysis of Section 3, it can be concluded that, if the VTL is used to track the PRPS with the architecture of a continuous CDMA signal, the performance of the VTL will degrade due to the signal structure difference. To solve the problems in tracking PRPS, an optimized VTL architecture that includes irregular update periods (IUP) pre-filters and a navigation filter based on predicted measurements (PM) is proposed. This section first presents the architecture of the IUPPM-VTL and then discusses the discrete-time models of the pre-filter and the navigation filter.

4.1. Architecture of the IUPPM-VTL

Figure 5 shows the block diagram of the IUPPM-VTL. The pulse control module generates the pulse signal $H^i(t)$ and calculates intervals T_{k-1} between two adjacent active timeslots according to the predetermined pseudo-random permutation. The Integrate and Dump (I&D) module only integrates during the active timeslots, avoiding interference of other PRPS. The discriminator outputs the carrier phase error $\Delta\phi_k$ and the code phase error $\Delta\tau_k$. Then, the IUP pre-filter based KF filters $\Delta\phi_k$ and $\Delta\tau_k$ in irregular periods according to the intervals T_{k-1} . Meanwhile, the estimated errors of the pre-filter are the inputs of the navigation filter. The input measurements are firstly predicted to ensure the same sampling time. Thus, it will not lead to performance degradation due to inconsistent input sampling times. Finally, the corrections estimated by EKF are used to adjust the channel NCO through the line of sight (LOS) projection.

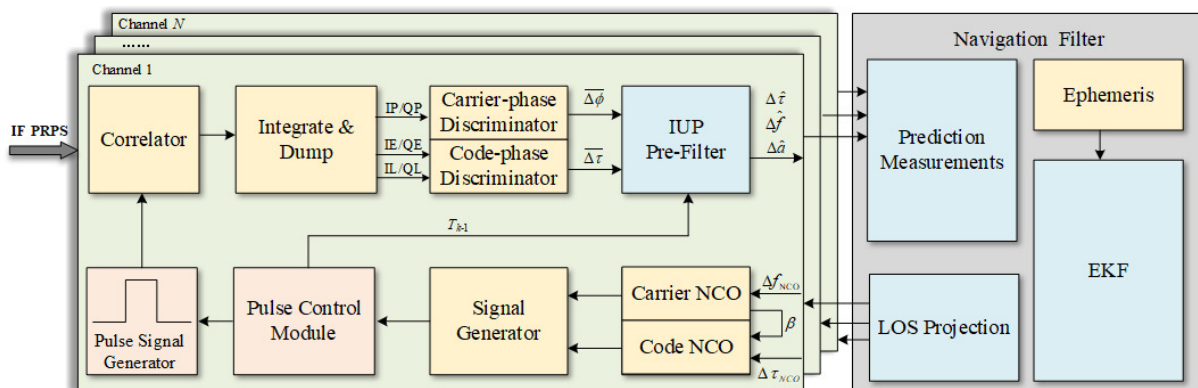


Figure 5. Block diagram of the IUPPM-VTL.

4.2. Pre-Filter Model

Because the update period of the states in KF can be time-varying, while that in PLL and DLL can only be fixed, the KF structure is adopted for the IUP pre-filter.

The state vector of linear KF describes the system time evolution [40] and is typically defined as an error vector of four parameters: code phase error $\Delta\tau$ (unit: chips), carrier phase $\Delta\phi$ (unit: radians), carrier frequency error Δf (unit: Hz), and carrier frequency rate error Δa (unit: Hz/s). The state vector at the k -th active timeslot can be described as:

$$\Delta X_{k,1} = [\Delta\tau, \Delta\phi, \Delta f, \Delta a]_k^T, \quad (13)$$

where subscript 1 indicates the pre-filter.

The dynamic system model is related to the intervals, described in Equation (11).

$$\Delta X_{k,1} = F_{k,1} \cdot \Delta X_{k-1,1} + \mathbf{w}_{k-1,1}, \quad (14)$$

where $F_{k,1}$ denotes the state transition matrix [39,41] as:

$$F_{k,1} = \begin{bmatrix} 1 & 0 & \beta T_{k-1} & \frac{1}{2}\beta T_{k-1}^2 \\ 0 & 1 & 2\pi T_{k-1} & \pi T_{k-1}^2 \\ 0 & 0 & 1 & T_{k-1} \\ 0 & 0 & 0 & 1 \end{bmatrix}_k. \quad (15)$$

It should be emphasized that T_{k-1} is not constant. Instead, it is calculated according to the pseudo-random active timeslot intervals, avoiding the inaccurate output model of the discriminators, as described in Section 3.

In Equation (14), $\mathbf{w}_{k-1,1}$ indicates the process noise vector, and its covariance matrix is $\mathbf{Q}_{k-1,1}$ which can be described as [39,40]:

$$\mathbf{Q}_{k-1,1} = \mathbf{Q}_{code} + \mathbf{Q}_{LOS} + \mathbf{Q}_p + \mathbf{Q}_f, \quad (16)$$

where

$$\mathbf{Q}_{code} = q_{code} \begin{bmatrix} T_{k-1} & 0 & 0 & 0 \\ 0 & 0 & 0 & 0 \\ 0 & 0 & 0 & 0 \\ 0 & 0 & 0 & 0 \end{bmatrix}, \quad \mathbf{Q}_{LOS} = q_{LOS} \begin{bmatrix} \frac{T_{k-1}^5}{20}\beta^2 & \frac{T_{k-1}^5}{20}\beta^2 & \frac{T_{k-1}^4}{8}\beta & \frac{T_{k-1}^3}{6}\beta \\ \frac{T_{k-1}^5}{20}\beta^2 & \frac{T_{k-1}^5}{20}\beta^2 & \frac{T_{k-1}^4}{8}\beta & \frac{T_{k-1}^3}{6}\beta \\ \frac{T_{k-1}^4}{8}\beta & \frac{T_{k-1}^4}{8}\beta & \frac{T_{k-1}^3}{3} & \frac{T_{k-1}^2}{2} \\ \frac{T_{k-1}^3}{6}\beta & \frac{T_{k-1}^3}{6}\beta & \frac{T_{k-1}^2}{2} & T_{k-1} \end{bmatrix}, \quad (17)$$

$$\mathbf{Q}_p = S_p \omega_{RF}^2 \cdot \begin{bmatrix} T_{k-1}\beta^2 & T_{k-1}\beta & 0 & 0 \\ T_{k-1}\beta & T_{k-1} & 0 & 0 \\ 0 & 0 & 0 & 0 \\ 0 & 0 & 0 & 0 \end{bmatrix}, \quad \mathbf{Q}_f = S_f \omega_{RF}^2 \cdot \begin{bmatrix} \frac{T_{k-1}^3}{3}\beta^2 & \frac{T_{k-1}^3}{3}\beta & \frac{T_{k-1}^2}{2}\beta & 0 \\ \frac{T_{k-1}^3}{3}\beta & \frac{T_{k-1}^3}{3} & \frac{T_{k-1}^2}{2} & 0 \\ \frac{T_{k-1}^2}{2}\beta & \frac{T_{k-1}^2}{2} & T_{k-1} & 0 \\ 0 & 0 & 0 & 0 \end{bmatrix}, \quad (18)$$

where q_{LOS} represents the random walk process driving the line-of-sight acceleration, q_{code} represents the code/carrier divergence, and S_p and S_f denote the phase and frequency random walk power spectral density due to the receiver oscillator, respectively. ω_{RF} is the carrier frequency. Given the oscillator h-parameters, the clock noise spectral densities are obtained as [39,42]:

$$\begin{aligned} S_p &= \frac{1}{2}h_0 \\ S_f &= 2\pi^2 h_{-2} \end{aligned}. \quad (19)$$

The discriminator outputs of the code phase $\overline{\Delta\tau}$ and the carrier phase $\overline{\Delta\phi}$ are used as the measurements in the pre-filter. So, the measurement vector $\mathbf{Z}_{k,1}$ is:

$$\mathbf{Z}_{k,1} = [\overline{\Delta\tau}, \overline{\Delta\phi}]_k^T. \quad (20)$$

The measurement model can be expressed as follows:

$$\mathbf{Z}_{k,1} = \mathbf{H}_1 \cdot \Delta \mathbf{X}_{k,1} + \mathbf{v}_{k,1}, \quad (21)$$

where \mathbf{v}_k is the measurement noise, and its covariance matrix $\mathbf{R}_{k,1}$ is

$$\mathbf{R}_{k,1} = \begin{bmatrix} \sigma_{\Delta\tau}^2 & 0 \\ 0 & \sigma_{\Delta\phi}^2 \end{bmatrix}, \quad (22)$$

where $\sigma_{\Delta\tau}^2$ and $\sigma_{\Delta\phi}^2$ are the noise standard deviations of the code phase and carrier phase discriminator outputs, respectively. The early minus late envelope and the four-quadrant arctangent are selected as code and carrier discriminators. The measurement variances for the above discriminators are given by Reference [39,41]:

$$\sigma_{\Delta\tau}^2 = \frac{d}{4C/N_0 \cdot T_s} \cdot \left[1 + \frac{2}{(2-d)C/N_0 \cdot T_s} \right], \quad (23)$$

$$\sigma_{\Delta\phi}^2 = \frac{1}{2C/N_0 \cdot T_s} \cdot \left(1 + \frac{1}{2C/N_0 \cdot T_s} \right), \quad (24)$$

where d is the spacing between early and late replica codes, and C/N_0 is the carrier-to-noise ratio.

The relationship between the states and the measurements can be modeled as follows:

$$\begin{aligned} \overline{\Delta\tau_k} &= \frac{1}{T_s} \int_{T_{k-1}}^{T_{k-1}+T_s} \left(\Delta\tau_{k-1} + \beta\Delta f_{k-1}t + \frac{1}{2}\beta\Delta a_{k-1}t^2 \right) dt \\ &= \Delta\tau_k - \frac{1}{2}\beta\Delta f_k T_s + \frac{1}{6}\beta\Delta a_k T_s^2 \end{aligned}, \quad (25)$$

$$\begin{aligned} \overline{\Delta\phi_k} &= \frac{1}{T_s} \int_{T_{k-1}}^{T_{k-1}+T_s} \left(\Delta\phi_{k-1} + 2\pi\Delta f_{k-1}t + \pi\Delta a_{k-1}t^2 \right) dt \\ &= \Delta\phi_k - \pi\Delta f_k T_s + \frac{1}{3}\pi\Delta a_k T_s^2 \end{aligned}. \quad (26)$$

According to Equations (13), (25), and (26), the measurement model can be reconstructed as:

$$\begin{bmatrix} \overline{\Delta\tau_k} \\ \overline{\Delta\phi_k} \end{bmatrix}_k = \begin{bmatrix} 1 & 0 & -\frac{1}{2}\beta T_s & \frac{1}{6}\beta T_s^2 \\ 0 & 1 & -\pi T_s & \frac{1}{3}\pi T_s^2 \end{bmatrix} \cdot \begin{bmatrix} \Delta\tau \\ \Delta\phi \\ \Delta f \\ \Delta a \end{bmatrix}_k + \mathbf{v}_{k,1}. \quad (27)$$

Thus, the observation matrix \mathbf{H}_1 in Equation (21) is

$$\mathbf{H}_1 = \begin{bmatrix} 1 & 0 & -\frac{1}{2}\beta T_s & \frac{1}{6}\beta T_s^2 \\ 0 & 1 & -\pi T_s & \frac{1}{3}\pi T_s^2 \end{bmatrix}. \quad (28)$$

After establishing the dynamic and measurement models, the KF including one-step prediction and measurement correction can be implemented [40].

- Prediction

$$\begin{aligned} \Delta \hat{\mathbf{X}}_{k|k-1,1} &= \mathbf{F}_{k,1} \cdot \Delta \hat{\mathbf{X}}_{k-1,1} \\ \mathbf{P}_{k|k-1,1} &= \mathbf{F}_{k,1} \cdot \mathbf{P}_{k-1,1} \cdot \mathbf{F}_{k,1}' + \mathbf{Q}_{k-1,1}' \end{aligned} \quad (29)$$

where $\Delta \hat{\mathbf{X}}_{k|k-1,1}$ is the priori state estimation, and $\mathbf{P}_{k|k-1,1}$ is the priori estimation covariance matrix calculated by projecting the error covariance ahead.

- Correction

$$\mathbf{K}_{k,1} = \mathbf{P}_{k|k-1,1} \mathbf{H}_{k,1}^T \left(\mathbf{H}_{k,1} \mathbf{P}_{k|k-1,1} \mathbf{H}_{k,1}^T + \mathbf{R}_{k,1} \right)^{-1}, \quad (30)$$

$$\begin{aligned} \Delta \hat{\mathbf{X}}_{k,1} &= \Delta \hat{\mathbf{X}}_{k|k-1,1} + \mathbf{K}_{k,1} \left(\mathbf{Z}_{k,1} - \mathbf{H}_{k,1} \Delta \hat{\mathbf{X}}_{k|k-1,1} \right) \\ \mathbf{P}_{k,1} &= (\mathbf{I}_{4 \times 4} - \mathbf{K}_{k,1} \mathbf{H}_{k,1}) \mathbf{P}_{k|k-1,1} \end{aligned} \quad (31)$$

In Equations (30) and (31), $\mathbf{K}_{k,1}$ denotes KF gains, which is the weight of the difference between the received and predicted measurements. The KF gains are then exploited to estimate the posterior state estimation $\Delta \hat{\mathbf{X}}_{k,1}$ by including the measurement $\mathbf{Z}_{k,1}$. The posteriori estimation of the covariance matrix can be derived from $\mathbf{P}_{k|k-1,1}$. Finally, the posterior state estimations $\Delta \hat{\tau}_{k,1}$ and $\Delta \hat{f}_{k,1}$ of each channel are input into the navigation filter as measurements.

4.3. Navigation Filter Model

For PLPS, the posterior estimations of the pre-filter can only reflect the error before the end of the current active timeslot. Thus, there is likely to be a time difference among the measurements sampling time of the navigation filter, as shown in the gray shade in Figure 4. Moreover, since the active timeslot of each pseudolite is pseudo-random and does not overlap, the time difference is time-varying. If the posterior estimations of the pre-filter are directly utilized as the measurements of the navigation filter, the measurement errors will increase, reducing the tracking performance of VTL. A predicted measurements module is added into the navigation filter in this paper to solve this problem, as shown in Figure 5. The mathematical model of the predicted measurements module is described as follows.

$$\begin{aligned} \Delta \rho^i &= \lambda_c \cdot \left(\Delta \hat{\tau}_k^i + \beta \Delta \hat{f}_k^i \Delta t_k^i + \frac{1}{2} \beta \Delta \hat{a}_k^i \Delta t_k^i \right), \\ \Delta \dot{\rho}^i &= \lambda_r \cdot \left(\Delta \hat{f}_k^i + \Delta \hat{a}_k^i \Delta t_k^i \right) \end{aligned} \quad (32)$$

where the superscript i indicates the i -th channel. λ_c and λ_r are the wavelength of pseudorandom-code and radio frequency carrier, respectively. $\Delta \rho^i$ and $\Delta \dot{\rho}^i$ represent pseudo-range and pseudo-range rate errors that are the measurements of the navigation filter. Δt_k^i denotes the intervals between the update time of the pre-filter of each channel and the input sampling time of the navigation filter.

The measurement vector of the navigation filter is

$$\mathbf{Z}_{k,2} = \left[\Delta \rho^1, \Delta \rho^2, \dots, \Delta \rho^N, \Delta \dot{\rho}^1, \Delta \dot{\rho}^2, \dots, \Delta \dot{\rho}^N \right]_k^T, \quad (33)$$

where subscript 2 and k indicate the navigation filter and the k -th epoch.

The system state vector consists of eight errors and is described as

$$\Delta \mathbf{X}_{k,2} = [\Delta x, \Delta y, \Delta z, \Delta v_x, \Delta v_y, \Delta v_z, \Delta b, \Delta d]_{k,2}^T, \quad (34)$$

where Δx , Δy , Δz , and Δv_x , Δv_y , Δv_z are the receiver position and velocity errors, Δb and Δd are clock bias and drift errors. The system state can be described as a first-order Gauss-Markov process, which is given by

$$\Delta \mathbf{X}_{k,2} = \mathbf{F}_{k,2} \cdot \Delta \mathbf{X}_{k-1,2} + \mathbf{w}_{k,2}, \quad (35)$$

where $\mathbf{w}_{k,2}$ is process noise, and its covariance matrix is $\mathbf{Q}_{k-1,2}$. $\mathbf{F}_{k,2}$ is the transition matrix, which can be expressed as follows.

$$\mathbf{F}_{k-1,2} = \begin{bmatrix} \mathbf{I}_{3 \times 3} & T_f \cdot \mathbf{I}_{3 \times 3} & \mathbf{0}_{3 \times 2} \\ \mathbf{0}_{3 \times 3} & \mathbf{I}_{3 \times 3} & \mathbf{0}_{3 \times 2} \\ \mathbf{0}_{2 \times 3} & \mathbf{0}_{2 \times 3} & \mathbf{K} \end{bmatrix}_{8 \times 8}, \quad (36)$$

where T_f is the frame period of PRPS defined in Equation (3), $I_{3 \times 3}$ represents the third order identity matrix, and \mathbf{K} is

$$\mathbf{K} = \begin{bmatrix} 1 & T_f \\ 0 & 1 \end{bmatrix}. \quad (37)$$

The pseudorange equation can be modeled as follows for the i -th pseudolite.

$$\rho_k^i = r_k^i + b_k + n_k^i, \quad (38)$$

where ρ_k^i is the corrected pseudorange. b represents receiver clock bias. n_k^i represents pseudo-range noise. r_k^i indicates the distance between the receiver and pseudolite, which is given by

$$r_k^i = \sqrt{(x^i - x_k)^2 + (y^i - y_k)^2 + (z^i - z_k)^2}, \quad (39)$$

where x^i , y^i , and z^i represent the position of i -th pseudolite. x_k , y_k , z_k indicates the receiver position at k -th epoch. Because pseudolites are built on the ground, this paper assumes that their positions are fixed. Therefore, the navigation filter can omit the process of estimating the pseudolite position during every epoch.

At epoch k , a first-order Taylor's expansion is used to linearize the relationship between the state and measurement vectors. According to Equations (38) and (39), $\Delta\rho_k^i$ is

$$\Delta\rho_k^i = -l_{x,k}^i \cdot \Delta x_k - l_{y,k}^i \cdot \Delta y_k - l_{z,k}^i \cdot \Delta z_k + \Delta b_k, \quad (40)$$

where $l_k^i = [l_{x,k}^i, l_{y,k}^i, l_{z,k}^i]^T$ is the LOS projection from the receiver to i -th pseudolite and can be expressed as:

$$\begin{cases} l_{x,k}^i = (x^i - x_k) / r_k^i \\ l_{y,k}^i = (y^i - y_k) / r_k^i \\ l_{z,k}^i = (z^i - z_k) / r_k^i \end{cases}. \quad (41)$$

Similarly, the pseudorange-rate error $\Delta\rho_k^i$ is given by

$$\Delta\rho_k^i = -l_k^i \cdot \Delta v_k + \Delta d_k, \quad (42)$$

where $v_k = [\Delta v_x, \Delta v_y, \Delta v_z]^T_k$.

According to Equations (40) and (42), the measurement equation can be obtained as:

$$\mathbf{Z}_{k,2} = \mathbf{H}_{k,2} \cdot \Delta\mathbf{X}_{k,2} + \mathbf{v}_{k,2}, \quad (43)$$

where $\mathbf{v}_{k,2}$ is the measurement noise, and its covariance matrix is $R_{k,2}$. The measurement matrix $\mathbf{H}_{k,2}$ is given by

$$\mathbf{H}_{k,2} = \begin{bmatrix} -l_x^1 & -l_y^1 & -l_z^1 & 0 & 0 & 0 & 1 & 0 \\ -l_x^2 & -l_y^2 & -l_z^2 & 0 & 0 & 0 & 1 & 0 \\ \vdots & \vdots \\ -l_x^N & -l_y^N & -l_z^N & 0 & 0 & 0 & 1 & 0 \\ 0 & 0 & 0 & -l_x^1 & -l_y^1 & -l_z^1 & 0 & 1 \\ 0 & 0 & 0 & -l_x^2 & -l_y^2 & -l_z^2 & 0 & 1 \\ \vdots & \vdots \\ 0 & 0 & 0 & -l_x^N & -l_y^N & -l_z^N & 0 & 1 \end{bmatrix}_{2N \times 8}. \quad (44)$$

Then, the posterior pseudorange and pseudorange-rate error estimations $\Delta\hat{\mathbf{Y}}_k$ can be achieved by:

$$\Delta\mathbf{Y}_k = \mathbf{H}_{k,2} \cdot \Delta\mathbf{X}_{k,2}. \quad (45)$$

The feedback corrections to the NCO of each channel is calculated as follows:

$$\begin{aligned}\Delta\tau_{\text{NCO},k}^i &= (\hat{\rho}_k^i - \tilde{\rho}_k^i) / \lambda_c \\ \Delta f_{\text{NCO},k}^i &= (\hat{\dot{\rho}}_k^i - \tilde{\dot{\rho}}_k^i) / \lambda_r\end{aligned}\quad (46)$$

where $\hat{\rho}_k^i$ and $\tilde{\rho}_k^i$ are the estimated and measured pseudo-range at k -th epoch. $\hat{\dot{\rho}}_k^i$ and $\tilde{\dot{\rho}}_k^i$ are the estimated and measured pseudo-range rate at k -th epoch.

The process of the PM navigation filtering can be summarized as follows, based on the system dynamic and measurement models established above.

- Step1: Predict the measurements according to Equation (32) so that they can be sampled at the same time.
- Step2: Estimate the priori state: $\Delta\hat{\mathbf{X}}_{k|k-1,2} = \mathbf{F}_{k,2} \cdot \Delta\hat{\mathbf{X}}_{k-1,2}$.
- Step3: Calculate the priori estimation covariance: $\mathbf{P}_{k|k-1,2} = \mathbf{F}_{k,2} \cdot \mathbf{P}_{k-1,2} \cdot \mathbf{F}_{k,2} + \mathbf{Q}_{k-1,2}$.
- Step4: Calculate the Kalman gain: $\mathbf{K}_{k,2} = \mathbf{P}_{k|k-1,2} \mathbf{H}_{k,2}^T (\mathbf{H}_{k,2} \mathbf{P}_{k|k-1,2} \mathbf{H}_{k,2}^T + \mathbf{R}_{k,2})^{-1}$.
- Step5: Estimate the posterior state: $\Delta\hat{\mathbf{X}}_{k,2} = \Delta\hat{\mathbf{X}}_{k|k-1,2} + \mathbf{K}_{k,2} (\mathbf{Z}_{k,2} - \mathbf{H}_{k,2} \Delta\hat{\mathbf{X}}_{k|k-1,2})$.
- Step6: Compute the posterior estimation covariance: $\mathbf{P}_{k,2} = (\mathbf{I}_{8 \times 8} - \mathbf{K}_{k,2} \mathbf{H}_{k,2}) \mathbf{P}_{k|k-1,2}$.
- Step7: LOS Projection: $\Delta\hat{\mathbf{Y}}_k = \mathbf{H}_{k,2} \cdot \Delta\hat{\mathbf{X}}_{k,2}$.
- Step8: Feedback to NCO: as described in Equation (46).

5. Simulation and Results

In this section, a simulation is carried out to compare the performance of the proposed IUPPM-VTL with traditional VTL and IUP-VTL.

5.1. Simulation Setup

Figure 6 shows the block diagram of the self-developed simulation scheme. First, the position and velocity of the receiver are preset in the trajectory generator. Then, the IF PRPS can be produced according to the fixed pseudolite position. This paper assumes that there is no multipath signal and that the pseudolite net is synchronous. Therefore, the PRPS is transmitted through the Gaussian channel, and it will be captured and tracked by the receiving module. Finally, the position, velocity, doppler, and code phase error results are used to evaluate the performance of different vector tracking structures.

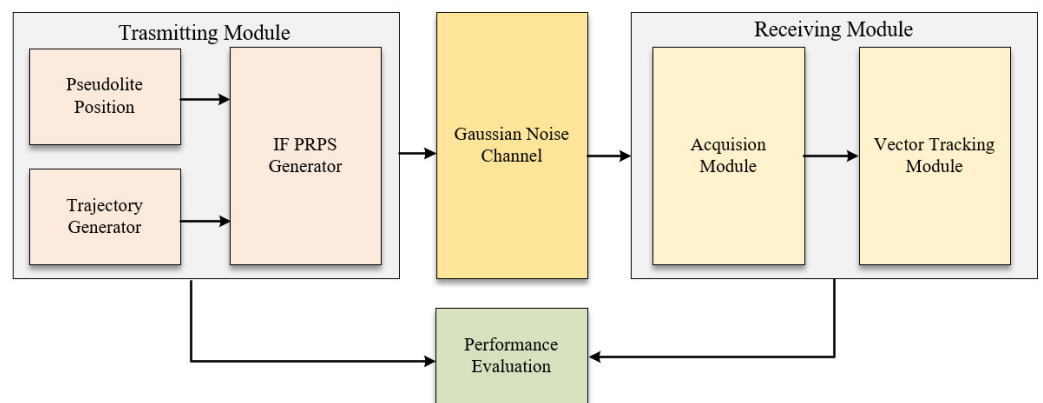


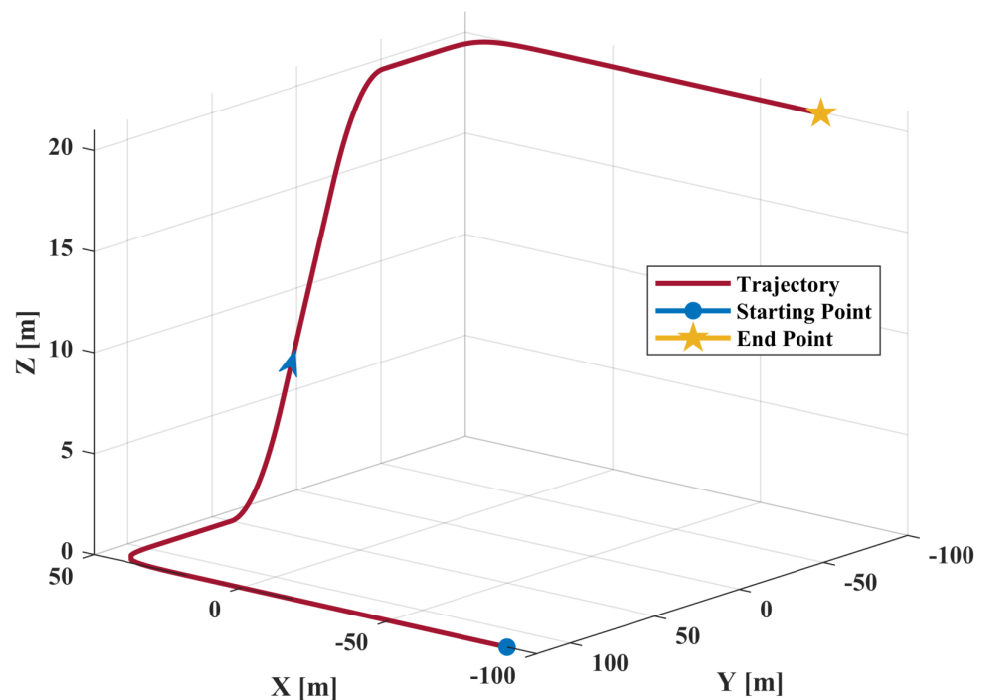
Figure 6. Block diagram of the simulation scheme.

The simulation in this paper is established on a self-defined XYZ coordinate system. This process does not affect the evaluation of vector tracking performance but avoids the transformation between coordinate systems. The parameters of the PRPS are listed in Table 1. The total number of pseudolite is 10 in the simulation.

Table 1. Main parameters of PRPS.

RF (f_c)	1575.42 MHz
IF (f_{IF})	24 MHz
code frequency	10.23 MHz
code length	1023 chips
duty cycle of the pulse pattern (d)	0.1
Timeslot Period (T_s)	0.1 ms
Frame Period (T_f)	1 ms
Number of Timeslots in one Frame (N_s)	10
Number of Frames (N_f)	200
Super Frame Period (T_p)	200 ms

The reference trajectory is shown in Figure 7, the blue dot is the starting point, the blue arrow represents the direction of motion, and the yellow five-pointed star is the endpoint. The reference velocity and acceleration are presented in Figure 8a,b, respectively.

**Figure 7.** Reference trajectory.

The dynamic process of the receiver is described as follows:

1. The receiver is in a static state during 0~7 s, and the relative coordinate of the starting point is $[-90, 120, 0]$ (m).
2. Conduct a constant acceleration movement in the $+x$ direction with an acceleration of 10 m/s and a duration of 2 s.
3. Stop acceleration and maintain a constant velocity state for 1 s.
4. Make a 1/4 circular motion with a circle radius of 50 m.
5. The receiver moves toward the $-y$ direction and keeps moving at a constant speed for 1.382 s.
6. Apply a constant acceleration in the $+z$ direction. The acceleration is 10 m/s, and the duration is 1 s.
7. Stop acceleration and maintain a constant velocity state for 1 s.
8. Perform a deceleration movement in the $+z$ direction until $V_z = 0$ and the acceleration is -10 m/s.

9. Keep a uniform speed in the $-y$ direction for 1 s.
10. Make a 1/4 circular motion with a circle radius of 50 m.
11. The receiver moves toward the $-x$ direction and keeps moving at a constant speed for 1.382 s.
12. Perform a deceleration movement in the $-x$ direction until $V_x = 0$ and the acceleration is -10 m/s.
13. The receiver remains stationary for 3 s.

The dynamic process described above lasts for a total time of 30 s and the coordinate of end point is $[-71.5, -98.3, 20.0]$ (m).

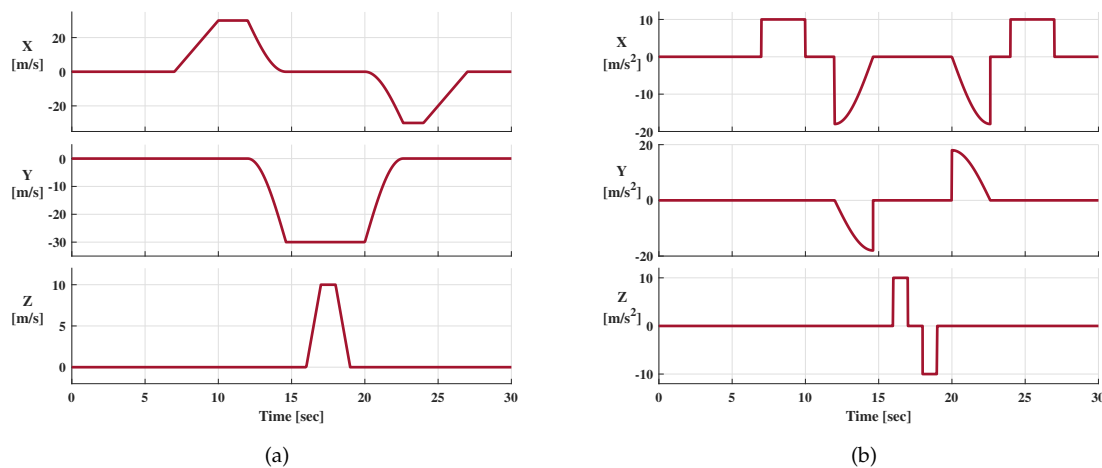


Figure 8. Reference dynamic. (a) Reference velocity. (b) Reference acceleration.

5.2. Simulation Results

This paper pays more attention to the influence of the PLPS on tracking and position accuracy, weakening the impact of factors, such as the received signal power fluctuation, with the distance variation. Thus, the received signal power is set as fixed. The carrier-to-noise ratio (C/N_0) of IF PRPS is set to $50 \text{ dB} \cdot \text{Hz}$ in this simulation scenario. Next, three different VTL structures are applied to track the preset IF PRPS. Finally, the tracking and navigation results are analyzed and compared.

The tracking errors of VTL mainly refer to doppler error and code phase error, which are obtained by the difference between the local replica signal and the received signal. Figures 9 and 10 shows the tracking errors of the 10th-Pseudolite. The blue, yellow, and red lines represent the position errors of VTL, IUP-VTL, and IUPPM-VTL algorithms, respectively. The dashed box shown in Figure 9 describes the peak caused by sudden changes in acceleration. From the enlarged view, it can be seen that the IUPPM-VTL can respond to acceleration changes faster. The root mean square errors (RMSE) of doppler and code phase are calculated and recorded in Table 2. It is illustrated that the IUPPM-VTL has the best tracking accuracy throughout the tracking process. The tracking results of all pseudolites are demonstrated in Figure 11a,b.

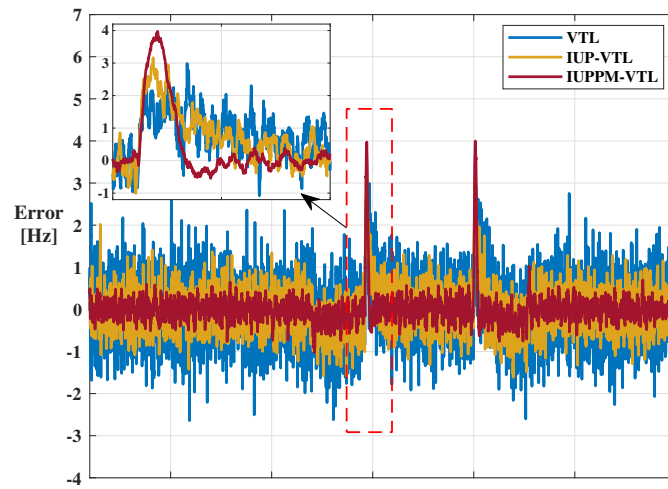


Figure 9. Doppler error of the 10th-Pseudolite.

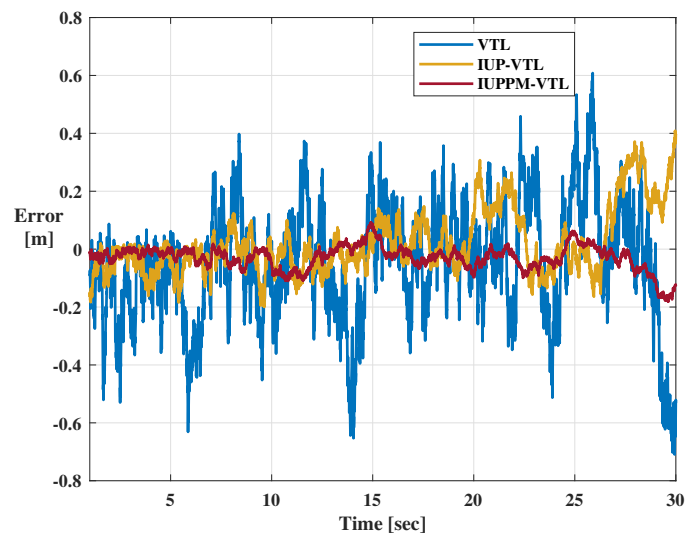


Figure 10. Code phase error of the 10th-Pseudolite.

Table 2. Comparison of doppler and code phase errors of the 10th-Pseudolite.

RMSE	VTL	IUP-VTL	IUPPM-VTL
Doppler [Hz]	0.7001	0.5218	0.5073
Code Phase [m]	0.2097	0.1124	0.0505

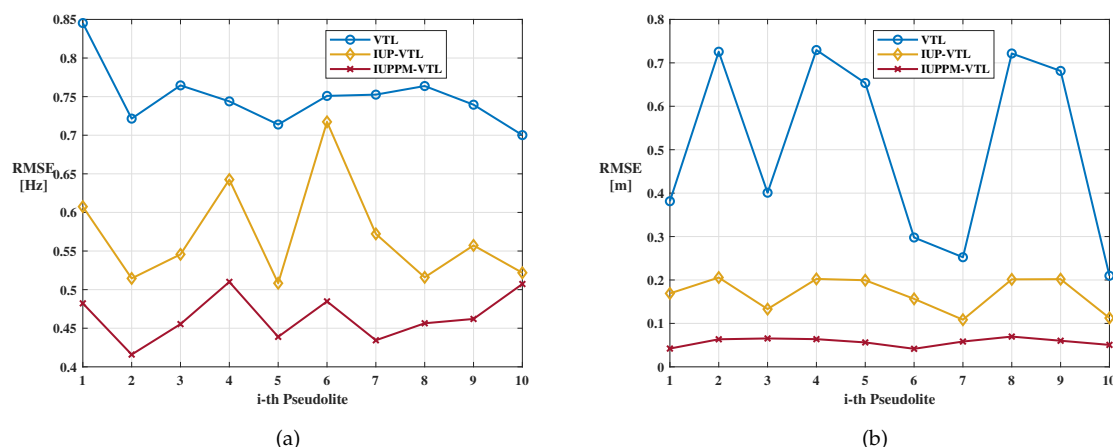


Figure 11. Tracking results of all pseudolites. (a) Doppler error of all pseudolites. (b) Code phase error of all pseudolites.

The position error is the difference between the position result and the reference trajectory shown in Figure 7. Figure 12 shows the position errors in XYZ directions. Because the IUPPM-VTL adopts a more accurate model, it performs a slighter jitter in position errors than VTL and IUP-VTL. The RMSEs of the position errors of VTL, IUP-VTL, and IUPPM-VTL are 0.63 m, 0.30 m, and 0.12 m, respectively. Hence, the proposed IUPPM-VTL performs best in position precision.

The velocity error is the difference between the velocity result and the reference velocity shown in Figure 8. Figure 13 shows the velocity errors in XYZ directions. The enlarged views of the solid line boxes demonstrate the velocity errors at the steady-state. The velocity errors at the abrupt acceleration in the X and Y directions are shown in the dotted box (details are shown in the enlarged version). When adopting the IUPPM-VTL, the sudden change in acceleration has a shorter disturbance time to the speed estimation than VTL and IUP-VTL because the proposed IUPPM-VTL has higher doppler tracking accuracy and more robust acceleration response capability. The RMSEs of the velocity errors of VTL, IUP-VTL, and IUPPM-VTL are 0.50 m/s, 0.40 m/s, and 0.24 m/s, respectively. Thus, the proposed IUPPM-VTL significantly improves velocity accuracy.

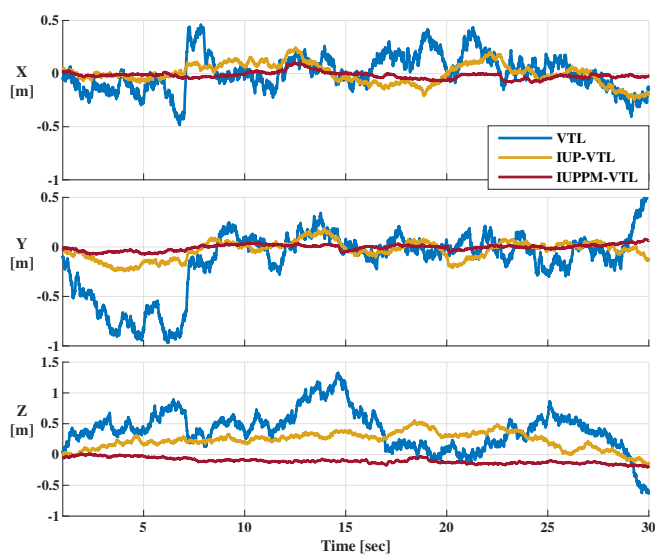


Figure 12. Position errors of three VTL structures in XYZ directions.

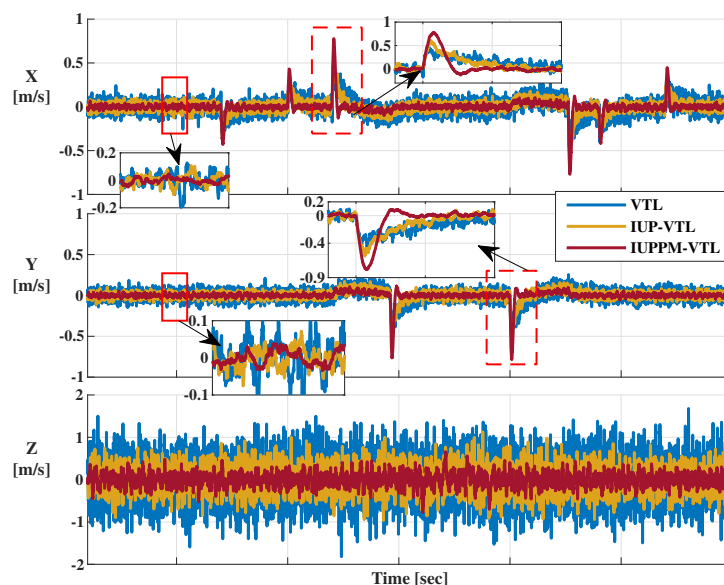


Figure 13. Velocity errors of three VTL structures in XYZ directions.

6. Conclusions

PLPS generally adopts a pseudo-random pulsing signal structure to mitigate the near-far effect. This signal pattern leads to irregular pulsing periods in the tracking loop when estimating the code phase, doppler, and carrier phase. However, traditional VTL is established on a continuous CDMA architecture. Thus, there exist two problems when directly adopting VTL to tracking PRPS.

- The discriminator model is affected by irregular pulsing periods in PLPS.
- The sampling time of the navigation filter inputs is inconsistent and time-varying in PLPS.

They will cause jitter degradation and biases in tracking PRPS. Thus, traditional VTL is incompatible with tracking PRPS.

Therefore, this paper proposes an optimized VTL architecture that includes IUP pre-filters and a navigation filter based on PM. According to the timeslot intervals, the IUP pre-filter based KF adjusts the update cycles, avoiding the impact of the pseudo-random pulsing signal. So, it can estimate the measurement accurately. Meanwhile, the navigation filter predicts the measurements of each pre-filter to the same sampling time. So, the measurements can reflect the errors of the sampling time, reducing the measurement noise of the navigation filter.

Additionally, a simulation test is carried out to compare the proposed IUPPM-VTL with traditional VTL based pre-filter and IUP-VTL based IUP-prefilter. The reference trajectory includes static, uniform acceleration, uniform speed, turning, and uniform deceleration. The maximum speed is 31.6 m/s, and the maximum acceleration is 18 m/s². Therefore, this comprehensive scenario can better evaluate the performance of the VTLs. The results show that the proposed IUPPM-VTL has a higher tracking accuracy than IUP-VTL and VTL. Meanwhile, their position errors are 0.12 m, 0.30 m, and 0.63 m, and their velocity errors are 0.24 m/s, 0.40 m/s, and 0.50 m/s. Thus, the proposed IUPPM-VTL performs the highest position and velocity precision among the three VTLs. In future work, it is necessary to concentrate on implementing and applying this method to real-time PRPS.

Author Contributions: Conceptualization, L.T.; methodology, L.T.; software, L.T.; validation, L.T. and G.L.; formal analysis, L.T.; investigation, L.T.; data curation, L.T., G.L., and J.S.; writing—original draft preparation, L.T.; writing—review and editing, L.T., G.L., J.S., and B.Z. All authors have read and agreed to the published version of the manuscript.

Funding: This research was funded by the National Key Research and Development Project of China grant number 2020YFB0505602-02.

Conflicts of Interest: The authors declare no conflict of interest.

References

1. Shoushtari, H.; Willemsen, T.; Sternberg, H. Many Ways Lead to the Goal—Possibilities of Autonomous and Infrastructure-Based Indoor Positioning. *Electronics* **2021**, *10*, 397. [[CrossRef](#)]
2. Chao, M.; Jinling, W.; Jianyun, C. Beidou Compatible Indoor Positioning System Architecture Design and Research on Geometry of Pseudolite. In Proceedings of the 2016 Fourth International Conference on Ubiquitous Positioning, Indoor Navigation and Location Based Services (UPINLBS), Shanghai, China, 2–4 November 2016; pp. 176–181.
3. Zidan, J.; Adegoke, E.I.; Kampert, E.; Birrell, S.A.; Ford, C.R.; Higgins, M.D. GNSS Vulnerabilities and Existing Solutions: A Review of the Literature. *IEEE Access*. **2020**, *4*, 1–17. [[CrossRef](#)]
4. Han, S.; Gong, Z.; Meng, W.; Li, C.; Gu, X. Future Alternative Positioning, Navigation, and Timing Techniques: A Survey. *IEEE Wirel. Commun.* **2016**, *23*, 154–160. [[CrossRef](#)]
5. Yao, Z.; Lu, M. Spreading modulation techniques in satellite navigation. In *Next-Generation GNSS Signal Design*; Springer: Singapore, 2021; pp. 89–162.
6. Yao, Z.; Lu, M.; Feng, Z.M. Quadrature multiplexed BOC modulation for interoperable GNSS signals. *Electron. Lett.* **2010**, *46*, 1234–1236. [[CrossRef](#)]
7. Gao, G.X.; Sgammini, M.; Lu, M.Q.; Kubo, N. Protecting GNSS Receivers From Jamming and Interference. *Proc. IEEE* **2016**, *104*, 1327–1338. [[CrossRef](#)]
8. Yassin, A.; Nasser, Y.; Awad, M.; Al-Dubai, A.; Liu, R.; Yuen, C.; Raulefs, R.; Aboutanios, E. Recent Advances in Indoor Localization: A Survey on Theoretical Approaches and Applications. *IEEE Commun. Surv. Tutor.* **2017**, *19*, 1327–1346. [[CrossRef](#)]
9. Gezici, S.; Poor, H.V. Position estimation via ultra-wide-band signals. *Proc. IEEE* **2009**, *97*, 386–403. [[CrossRef](#)]
10. Xie, T.; Jiang, H.J.; Zhao, X.J.; Zhang, C. A Wi-Fi-Based Wireless Indoor Position Sensing System with Multipath Interference Mitigation. *Sensors* **2019**, *19*, 3983. [[CrossRef](#)]
11. Peral-Rosado, J.; Lopez-Salcedo, J.; Seco-Granados, G. Impact of frequency-hopping NB-IoT positioning in 4G and future 5G networks. In Proceedings of the 2017 IEEE International Conference on Communications Workshops (ICC Workshops), Paris, France, 21–25 May 2017; pp. 815–820.
12. Politi, N.; Yong, L.; Faisal, K. Locata: A new technology for high precision positioning. In Proceedings of the European Navigation Conference, Naples, Italy, 3–6 May 2009; pp. 176–181.
13. Kim, C.; So, H.; Lee, T.; Kee, C. A pseudolite-based positioning system for legacy GNSS receivers. *Sensors* **2014**, *14*, 6104–6123. [[CrossRef](#)]
14. Li, X.; Zhang, P.; Huang, G.W.; Zhang, Q.; Guo, J.M.; Zhao, Y.Z.; Zhao, Q.Z. Performance analysis of indoor pseudolite positioning based on the unscented Kalman filter. *Gps Solut.* **2019**, *23*, 79. [[CrossRef](#)]
15. Cobb, H.S. GPS Pseudolites: Theory, Design, and Applications. Ph.D. Thesis, Stanford University, Stanford, CA, USA, 1997.
16. Liu, X.; Yao, Z.; Lu, M.Q. Robust time-hopping pseudolite signal acquisition method based on dynamic Bayesian network. *Gps Solut.* **2021**, *25*, 1–14. [[CrossRef](#)]
17. Elrod, B.D.; Van Dierendonck, A. Testing and evaluation of GPS augmented with pseudolites for precision approach applications. In Proceedings of the DSNs'93: 2nd International Symposium on Differential Satellite Navigation Systems, Amsterdam, The Netherlands, 29 March–2 April 1993; pp. 1269–1278.
18. Borio, D.; O'Driscoll, C. Design of a General Pseudolite Pulsing Scheme. *IEEE Trans. Aerosp. Electron. Syst.* **2014**, *50*, 2–16. [[CrossRef](#)]
19. Picois, A.V.; Samama, N. Near-Far Interference Mitigation for Pseudolites Using Double Transmission. *IEEE Trans. Aerosp. Electron. Syst.* **2014**, *50*, 2929–2941. [[CrossRef](#)]
20. Elrod, B.; Barltrop, K.; Stafford, J.; Brown, D. Test results of local area augmentation of GPS with an in-band pseudolite. In Proceedings of the 1996 National Technical Meeting of The Institute of Navigation, Santa Monica, CA, USA, 22–24 January 1996; pp. 145–154.
21. Barltrop, K.; Stafford, J.; Elrod, B.D. Local DGPS with pseudolite augmentation and implementation considerations for LAAS. In Proceedings of the 9th International Technical Meeting of the Satellite Division of The Institute of Navigation (ION GPS 1996), Kansas City, MO, USA, 17–20 September 1996; pp. 449–459.
22. Di, W. Design of a Pulsing Scheme for BeiDou Pseudolites Signals. In Proceedings of the 3rd International Conference on Transportation Information and Safety, Wuhan, China, 25–28 June 2015; pp. 542–547.
23. Tin Lian Abt, F.S.; Martin, S. Optimal Pulsing Schemes for Galileo Pseudolite Signals. *J. Glob. Position. Syst.* **2007**, *6*, 133–141.
24. Cheong, J.W.; Dempster, R.C.A.G. *Tracking of Time Hopped DS-CDMA Signals for Pseudolite-Based Positioning*; IGNSS Symposium: Surfers Paradise, Australia, 2009.
25. Yun, S.J.; Yao, Z.; Lu, M.Q. Variable update rate carrier tracking loop for time-hopping DSSS signals. *IET Radar Sonar Navig.* **2019**, *13*, 961–968. [[CrossRef](#)]
26. Wang, J.H.; Xu, Y.; Luo, R.D.; Zhang, Y.; Yuan, H. Synchronisation method for pulsed pseudolite positioning signal under the pulse scheme without slot-permutation. *IET Radar Sonar Navig.* **2017**, *11*, 1822–1830. [[CrossRef](#)]

27. Liu, K.; Guo, X.; Yang, J. Tracking loops with time-varying sampling periods for the TH-CDMA signal. In Proceedings of the 2016 IEEE International Conference on Signal and Image Processing (ICSIP), Beijing, China, 13–15 August 2016; pp. 508–513.
28. Spilker, J.J.; Parkinson, B. Fundamentals of signal tracking theory. *Prog. Astronaut. Aeronaut.* **1996**, *163*, 245–328.
29. Wang, H.; Cheng, Y.; Zhang, Y. Square-root cubature Kalman filter-based vector tracking algorithm in GPS signal harsh environments. *IET Radar Sonar Navig.* **2020**, *14*, 2027–2038. [[CrossRef](#)]
30. Dietmayer, K.; Kunzi, F.; Garzia, F.; Overbeck, M.; Felber, D. Real Time Results of Vector Delay Lock Loop in a Light Urban Scenario. In Proceedings of the 2020 IEEE/ION Position, Location and Navigation Symposium (PLANS), Portland, OR, USA, 20–23 April 2020; pp. 1230–1236.
31. Bhattacharyya, S. Performance and Integrity Analysis of the Vector Tracking Architecture of GNSS Receivers. Ph.D. Thesis, University of Minnesota, Minneapolis, MN, USA, 2012.
32. Matthew, L. Modeling and Performance Analysis of GPS Vector Tracking Algorithms. Ph.D. Thesis, Electrical Engineering, Auburn University, Auburn, AL, USA, 2009.
33. Chen, X.; Wang, X.; Xu, Y. Performance enhancement for a GPS vector-tracking loop utilizing an adaptive iterated extended Kalman filter. *Sensors* **2014**, *14*, 23630–23649. [[CrossRef](#)] [[PubMed](#)]
34. Alam, N.; Tian, J.; Khan, F.A. Theoretical Performance Analysis and Comparison of VDFLL and Traditional FLL Tracking Loops. In Proceedings of the 2018 European Navigation Conference (ENC), Gothenburg, Sweden, 14–17 May 2018; pp. 46–53.
35. Henkel, P.; Giger, K.; Gunther, C. Multifrequency, multisatellite vector phase-locked loop for robust carrier tracking. *IEEE J. Sel. Top. Signal Process.* **2009**, *3*, 674–681. [[CrossRef](#)]
36. So, H.; Lee, T.; Jeon, S.; Kim, C.; Kee, C.; Kim, T.; Lee, S. Implementation of a vector-based tracking loop receiver in a pseudolite navigation system. *Sensors* **2010**, *10*, 6324–6346. [[CrossRef](#)]
37. Jin, T.; Wang, C.; Lu, X.; Ling, K.V.; Cong, L. Analysis of a federal Kalman filter-based tracking loop for GPS signals. *GPS Solut.* **2019**, *23*, 1–13. [[CrossRef](#)]
38. Xie, F.; Sun, R.; Kang, G.; Qian, W.; Zhao, J.; Zhang, L. A jamming tolerant BeiDou combined B1/B2 vector tracking algorithm for ultra-tightly coupled GNSS/INS systems. *Aerosp. Sci. Technol.* **2017**, *70*, 265–276. [[CrossRef](#)]
39. O’Driscoll, C.; Petovello, M.G.; Lachapelle, G. Choosing the coherent integration time for Kalman filter-based carrier-phase tracking of GNSS signals. *GPS Solut.* **2010**, *15*, 345–356. [[CrossRef](#)]
40. Brown, R.G.; Hwang, P.Y. *Introduction to Random Signals and Applied Kalman Filtering: With MATLAB Exercises*; John Wiley & Sons: Hoboken, NJ, USA, 2012.
41. Susi, M.; Andreotti, M.; Aquino, M.; Dodson, A. Tuning a Kalman filter carrier tracking algorithm in the presence of ionospheric scintillation. *GPS Solut.* **2017**, *21*, 1149–1160. [[CrossRef](#)]
42. Tang, X.; Falco, G.; Falletti, E.; Presti, L.L. Theoretical analysis and tuning criteria of the Kalman filter-based tracking loop. *GPS Solut.* **2015**, *19*, 489–503. [[CrossRef](#)]